A&A 521, A49 (2010)
DOI: 10.1051/0004-6361/201014006

Astronomy & Astrophysics

Evidence for magnetic flux cancelation leading to an ejective solar eruption observed by *Hinode*, *TRACE*, *STEREO*, and *SoHO*/MDI⋆

A. C. Sterling[1,⋆⋆], C. Chifor[2], H. E. Mason[2], R. L. Moore[1], and P. R. Young[3,4]

[1] NASA/Marshall Space Flight Center, VP62/Space Science Office, Huntsville, AL 35805, USA
e-mail: alphonse.sterling@nasa.gov
[2] Department of Applied Mathematics and Theoretical Physics, CMS, Wilberforce Road, Cambridge CB3 0WA, UK
e-mail: cristina.chifor@gmail.com
[3] George Mason University, 4400 University Drive, Fairfax, VA 22030, USA
[4] Space Science Division, Naval Research Laboratory, Washington, DC 20375, USA

Received 7 January 2010 / Accepted 19 March 2010

ABSTRACT

Aims. We study the onset of a solar eruption involving a filament ejection on 2007 May 20.
Methods. We observe the filament in Hα images from *Hinode*/SOT and in EUV with *TRACE* and *STEREO*/SECCHI/EUVI. *Hinode*/XRT images are used to study the eruption in soft X-rays. From spectroscopic data taken with *Hinode*/EIS we obtain bulk-flow velocities, line profiles, and plasma densities in the onset region. The magnetic field evolution was observed in *SoHO*/MDI magnetograms.
Results. We observed a converging motion between two opposite polarity sunspots that form the primary magnetic polarity inversion line (PIL), along which resides filament material before eruption. Positive-flux magnetic elements, perhaps moving magnetic features (MMFs) flowing from the spot region, appear north of the spots, and the eruption onset occurs where these features cancel repeatedly in a negative-polarity region north of the sunspots. An ejection of material observed in Hα and EUV marks the start of the filament eruption (its "fast-rise"). The start of the ejection is accompanied by a sudden brightening across the PIL at the jet's base, observed in both broad-band images and in EIS. Small-scale transient brightenings covering a wide temperature range (Log T_e = 4.8−6.3) are also observed in the onset region prior to eruption. The preflare transient brightenings are characterized by sudden, localized density enhancements (to above Log n_e [cm^{-3}] = 9.75, in Fe XIII) that appear along the PIL during a time when pre-flare brightenings were occurring. The measured densities in the eruption onset region outside the times of those enhancements decrease with temperature. Persistent downflows (red-shifts) and line-broadening (Fe XII) are present along the PIL.
Conclusions. The array of observations is consistent with the pre-eruption sheared-core magnetic field being gradually destabilized by evolutionary tether-cutting flux cancelation that was driven by converging photospheric flows, and the main filament ejection being triggered by flux cancelation between the positive flux elements and the surrounding negative field. A definitive statement however on the eruption's ultimate cause would require comparison with simulations, or additional detailed observations of other eruptions occurring in similar magnetic circumstances.

Key words. Sun: filaments, prominences – Sun: coronal mass ejections (CMEs) – Sun: UV radiation – Sun: X-rays, gamma rays – Sun: flares

1. Introduction

Understanding the driver and trigger mechanisms for solar eruptions is a prominent issue in current solar physics research. It is widely accepted that solar eruptions are of magnetic origin; their manifestations include solar flares, filament eruptions and coronal mass ejections (CMEs). These phenomena play an important role in understanding, and ultimately predicting, space weather.

Regions that erupt are locations with enhanced magnetic fields, often an active region. In the low solar atmosphere the magnetic field pressure dominates the plasma pressure and gravitational forces, and so fundamentally the question is one of balance between between the magnetic elements involved, with (at least in simple bipole cases) downward-directed magnetic tension restraining the magnetic pressure trying to expand the field outward. For a given region, these forces can remain in balance for days or even weeks, as for example demonstrated sometimes by the presence of long-lived filaments residing on a polarity inversion line (PIL) of the region. Eventually however, the balance breaks down, and an eruption, often but not necessarily involving a filament, occurs along the PIL (e.g., Zirin 1988).

Several ideas have been advanced for the eruption onset mechanism. For the eruption to occur, the magnetic balance must be disrupted in favor of the upward-directed pressure force. Discussions of ideas for eruption onset mechanisms are presented in detail in several works and reviews, including van Driel-Gesztelyi et al. (2002); Klimchuk (2001); Linker et al. (2003); Forbes et al. (2006); Moore & Sterling (2006); van Driel-Gesztelyi (2009). Recently the consensus is that a "storage and release of energy" process occurs, where possible methods to release the energy are numerous.

We briefly recall a few of the proposed ideas here. "Tether cutting" is where magnetic tension restraining the sheared core

⋆ The video that accompanies Fig. 3 is only available in electronic form at http://www.aanda.org

⋆⋆ *Current address*: JAXA/Institute of Space and Astronautical Science, Hinode Group, Yoshinodai 3-1-1, chuo-ku, Sagamihara, Kanagawa, 252-5210, Japan.

field of a bipolar magnetic arcade is released by internal reconnection above the polarity inversion line of the arcade (e.g., Moore et al. 2001). "External tether cutting", or "breakout" reconnection, is similar to tether cutting in that it is a tension-release mechanism via reconnection, but here it occurs between the arcade envelope of the erupting field and an overarching, restraining, reversed field (Antiochos 1998; Antiochos et al. 1999). "Flux cancelation" (Martin et al. 1985), is when flux disappearance at the PIL leads to eruption; as formulated by van Ballegooijen & Martens (1989), this cancelation is due to reconnection, similar to the tether cutting idea, except in this case the emphasis is on the cancelation continuing over an extended period prior to eruption. "Current increase", for example via emergence of strongly-twisted flux ropes from below the surface (Leka et al. 1996), could also result in eruption (e.g., Amari et al. 2004). Another source for the onset of fast eruption is an "ideal MHD instability", for example driven by continued shearing of photospheric fields, where the fast eruption begins without pre-existing current sheets and reconnection (e.g., Kliem & Török 2006; Fan & Gibson 2007). Even in this case however, in most if not all events internal tether-cutting reconnection begins soon after the start of the fast eruption of the sheared core field and produces most of the event's particle acceleration and flare heating. There are rare "stealth" eruptions that produce a CME but have flare signatures that are very weak or absent, indicating weak or absent particle acceleration and plasma heating by reconnection (e.g. Hudson et al. 1998; Robbrecht et al. 2009).

Although the above mechanisms are often listed separately, even using numerical models it can in practice be difficult to disentangle which mechanism is actually responsible for fast eruption. Specifically, essentially all of the above-mentioned mechanisms lead to fast eruption only after the system is slowly evolved so that it no longer satisfies a stability criterion, and consequently erupts via an ideal MHD instability. For example, Aulanier et al. (2010) model the flux cancelation scenario, which leads to the eventual formation of a helical flux tube. But they conclude that photospheric flux cancelation alone is unlikely to produce eruption of the flux rope. Rather, the system actually erupts only after the system evolves to where a "torus instability" (Kliem & Török 2006; Isenberg & Forbes 2007) ensues. Thus in this case flux cancelation caused the system to evolve until the ideal MHD instability mechanism could take place.

Observationally, disentangling some of mechanisms can be an even greater challenge, as discussed in some detail by Moore & Sterling (2006). They conclude that two, or even all three mechanisms from among tether cutting, breakout, and ideal MHD instability, can be working in close succession or in tandem in leading to eruption onset, so that observationally it is often hard to distinguish exactly which mechanism is ultimately responsible for eruption onset. Moreover, Zhang et al. (2008) show that the relationship between flux emergence and eruptions is complex, and they conclude that the appearance of flux emergence alone is not unique for the initiation of CME eruption. That is, flux emergence, and perhaps cancelation, could be occurring frequently, but only leading to eruption when some other conditions are fulfilled.

Ultimately, we aim to know what conditions and processes are required for eruption in terms of the proposed or yet-to-be proposed mechanisms. This may differ from event to event. By studying individual case events, we hope to formulate a better understanding of the eruption process.

With the above background and cautions in mind, we proceed noting that Chifor et al. (2007) showed that preflare activity in the form of discrete, localized X-ray brightenings are

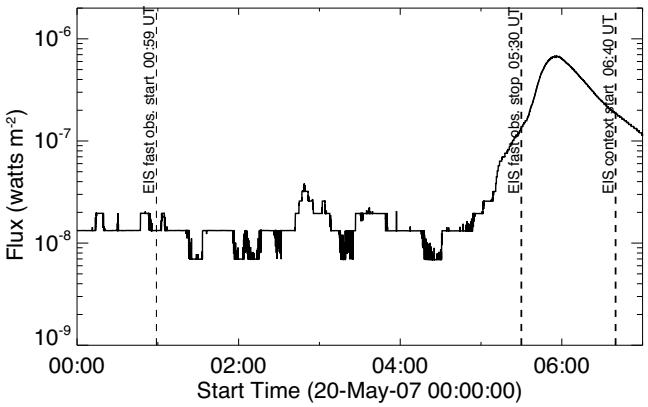

Fig. 1. Temporal X-ray evolution during the 2007 May 20 event measured by *GOES* in the 1–8 Å channel. Indicated on the figure are the times during which *Hinode*/EIS obtained the fast-cadence and the context raster observations.

precursors to filament eruptions, based on their observations of eight filament eruptions. They concluded that those events are evidence for a tether-cutting mechanism triggering the eruptions. Other studies have highlighted the importance of magnetic flux emergence or cancelation in triggering eruptions (e.g. Rust 1976; Heyvaerts et al. 1977; Sterling et al. 2007a).

Recent, advanced observations taken with the *Hinode* solar observatory can further our knowledge of the physical mechanisms responsible for solar eruptions (e.g., Sterling et al. 2007b; Su et al. 2007; Tan et al. 2009). In this paper we present a multi-wavelength analysis of a filament eruption observed with *Hinode* on 2007 May 20. Including complementary data from *SoHO*, *TRACE*, and *STEREO*, we study the physical mechanisms leading up to, and triggering the eruption.

As we will show, this event includes dynamic filament activity in the form of a surge jetting out along a main PIL of the region. The ejection occurs between positive and negative sunspot groups that had been converging for an extended period before eruption, and the foot of the surge was at a location were magnetic flux cancelation occurs, suggesting that the cancelation played an important role in the filament ejection and subsequent flaring onset. For our event, the preflare "activation" activity (activity starting prior to significant soft X-ray flare increase) includes the early-phase surge movement, and thus our findings are consistent with the cancelation resulting in this activation and triggering of the main eruption.

2. Overview of the instrumentation and data

The event was located in NOAA solar active region 10956 and produced a small flare of *GOES* class B6.7 starting at 04:52 UT and peaking at 05:56 UT on 2007 May 20 (Fig. 1). A white-light CME was first detected with *SoHO*/LASCO/C2 at 06:48 UT[1], having a linear speed of ~275 km s^{-1}. The same region produced an eruption on 2007 May 19 (see Sect. 8), although the topic of this paper is only the eruption of May 20.

The filament material that erupted was observed in images taken with *Hinode*/SOT (Solar Optical Telescope; Tsuneta et al. 2008) in Hα. This data set consisted of images obtained every 1 min between 04:00–05:46 UT with a spatial resolution of 0.16″/pixel. SOT used its narrow-band filter to observe in Hα, and so filtergraph magnetic data were not available for this study.

[1] http://lasco-www.nrl.navy.mil/cmelist.html

Table 1. Line list included in the "CAM_ARTB_RHESSI" observational sequence for EIS.

Ion	Wavelength (Å)	Log T_{max}* (K)	Note
Fe VIII	185.21	5.6	5.8, after Young et al. (2007a,b)
Fe XXIV	192.03	7.1	
Ca XVII	192.82	6.7	EIS core line
Fe XII	195.12	6.1	EIS core line
Fe XIII	202.0, 203.8	6.2	density pair (10^9–10^{11} cm−3)
He II	256.32	4.8	EIS core line
Si X	258.37, 261.0	6.1	density pair (10^7–10^{10} cm−3)
Fe XVI	262.98	6.4	
Fe XXIII	263.76	7.1	
Fe XIV	264.79, 274.2	6.2	density pair ($10^{8.5}$–10^{11} cm^{-3})
Mg VII	278.39, 280.75	5.8	density pair (10^9–10^{11} cm^{-3})
Fe XV	284.16	6.3	

Notes. (*) Temperature of the fractional ion population peak from Mazzotta et al. (1998).

Instead, we used data from MDI (Michelson Doppler Imager; Scherrer et al. 1995) aboard *SoHO* to measure the magnetic field over a period of several days.

A partial filament eruption was also observed in images from *TRACE* (*Transition Region and Coronal Explorer*; Handy et al. 1999) and from the SECCHI/EUVI (Sun Earth Connection Coronal and Heliospheric Investigation/Extreme UltraViolet Imager) instrument onboard the *STEREO* (*Solar TErrestrial RElations Observatory*; Wüelser et al. 2004) spacecraft (A and B). *TRACE* observations were obtained in the 171 Å filter (which has a peak response of ~1 MK), while SECCHI/EUVI observed in the 171 Å, 195 Å (~1.5 MK) and 304 Å (~60 000 K) filters. *TRACE* images have a cadence of 1 min and a pixel size of 0.5″. *STEREO* observed the full disk with a cadence of 2.5 min for the 171 Å images and 10 min for the 195 and 304 Å images. The EUVI spatial resolution was 1.59″/pixel. We observed the region in EUV with *STEREO* and *TRACE* from several hours prior to eruption, covering the preflare activity and entire event.

We analyzed images taken by *Hinode*/XRT (X-ray Telescope; Golub et al. 2007) through its "Ti_poly" filter, which is sensitive to plasmas mainly in the 2–5 MK range. We studied XRT images obtained between 04:00 UT and 08:00 UT, with a cadence of 30 s for most of the period and a pixel size of 1″.

Starting at 00:59 UT on May 20, *Hinode*/EIS (EUV Imaging Spectrometer; Culhane et al. 2007) ran the "CAM_ARTB_RHESSI" observing sequence consisting of a series of fast-cadence rasters until 05:30 UT followed by a context raster starting at 06:40 UT (Fig. 1). Data were not taken during the following periods when the satellite was in spacecraft night: 01:11–01:41 UT, 02:52–03:18 UT, 04:29–04:39 UT, 05:27–06:40 UT. EIS covers two wavelength bands: 170–211 Å and 246–292 Å, referred to as the short wavelength and the long wavelength bands, respectively. The "CAM_ARTB_RHESSI" sequence has been first reported by Chifor et al. (2008). This sequence was designed to investigate the small-scale, transient energy release in active regions. It includes a range of some of the strongest transition region and coronal lines observed with EIS covering a wide temperature range. The line list for this sequence is given in Table 1, with the temperatures of the fractional ion population peaks from Mazzotta et al. (1998). The hot Fe XXIV flare line at 192.03 Å is also covered. We note that according to Young et al. (2007a,b), Fe VIII seems to be formed at Log T_e = 5.8 rather than the temperature of log T (MK) = 5.6 as predicted by Mazzotta et al. (1998). Included in the sequence are line pairs (Mg VII λ278.39/λ280.75, Si X λ258.37/λ261.04, Fe XIII λ203.82/λ202.04, and Fe XIV λ264.79/λ274.20), which have density diagnostics capability (Young et al. 2007a,b). The fast cadence rasters (~3.5 min each) have a field of view (FOV) of 40″ × 120″, while the context raster (lasting ~20 min) has a wide FOV of 240″ × 240″. Both the context and the fast rasters use the 2″ EIS slit.

We calibrated the EIS line intensities in units of erg cm^{-2} s^{-1} sr^{-1} Å^{-1} at each pixel in the data set, by using the standard processing code *eis_prep* available in the SolarSoftWare (SSW) suite of software routines. We then fitted the spectrum obtained at each raster pixel with a Gaussian function using the SSW *eis_auto_fit* routine. To extract Doppler-shift information, one needs to correct for the EIS slit tilt, which is not perfectly vertical on the CCD. We obtained the slit tilt using the *eis_wave_corr* routine and then subtracted it from the fitted line center positions. Additionally, there is an orbital variation of the spectral line position due to the thermal changes across the instrument. This effect is usually determined by fitting a spline to the variation of the lines within the raster. In practice, the duration of the raster needs to be at least 10 min for this method to be applied. We note, however, that in the case of our fast rasters, with a cadence of ~3.5 min, the effect of the orbital variation should be small.

Both XRT and EIS images contain some pointing jitter due to small spacecraft motions, as well as orbital thermal changes that slightly modify the geometry of the instrument with respect to the spacecraft. The jitter is conspicuous particularly in the case of relatively small FOV images such as the fast-cadence EIS observations used in this analysis. To correct for both the jitter and orbital distortions in XRT images, one can use the SSW *xrt_jitter* routine, which makes the correction based on sun sensor signal information and an orbital variation model (Shimizu et al. 2007). We attempted to correct the jitter observed in the EIS movies, by interpolating the XRT offsets (east-west and north-south) to the times of the EIS observations. We shifted the EIS data sets by the resulting offsets, however this correction did not seem to remove the EIS jitter entirely. It is possible that there are further unknown small spacecraft motions, as well as orbital thermal changes related specifically to EIS, which the XRT correction does not account for. We note that the offsets are small, with the accuracy of this correction estimated at better than 5″.

To interpret the multi-wavelength observations, it is important to co-align the various data sets carefully. There is an instrumental offset between the images taken in the two EIS CCDs (Young et al. 2007b). To take this effect into account, we shifted

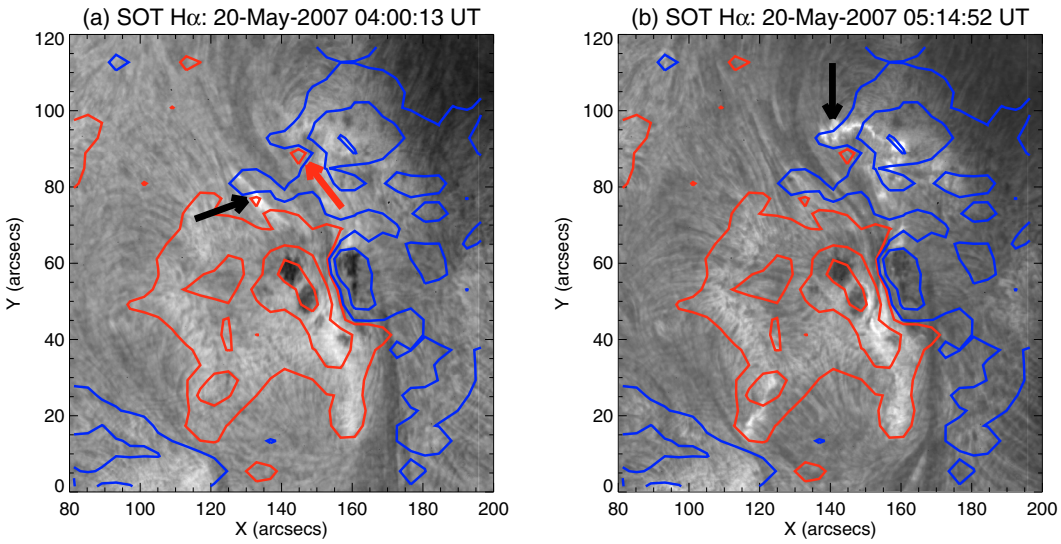

Fig. 2. *Hinode*/SOT Hα images with *SoHO*/MDI contours superimposed, showing the context of the observed sunspots, filament, and surrounding region. Red and blue contours are respectively the positive and negative polarities from an MDI magnetogram taken at 04:51 UT on May 20, with levels of 40, 300, and 750 G. Panel **a)** is from prior to eruption onset. The black arrow shows the brightening on part of the polarity inversion line, and the red arrow shows an "intruding" positive polarity in a surrounding negative region. Panel **b)** is from near the time of eruption onset, with the black arrow pointing to a ribbon occurring very close to the intruding positive polarity. We used the brightening and ribbon shown by black arrows respectively in panels **a)** and **b)** for aligning different data sets; for ease in identification in the text we call the indicated brightening the "4 UT brightening", as we refer to it several times. North is up and east is to the left in this and all solar images in this paper.

the long wavelength EIS CCDs data sets by 2″ in the solar x-direction and 17″ in the solar y-direction. A brightening before the eruption appeared at about 03:57 UT on part of the magnetic PIL across a wide temperature range (Log T_e = 4.8−6.3), being observed in all data sets (Hα, EUV and SXR). We used this brightening (see black arrow in Fig. 2a), to assist in co-alignment when overlaying the various data sets; below we refer to this brightening as the "4 UT brightening". Additionally, we used a ribbon-like feature that was observed in the SOT Hα images (black arrow in Fig. 2b) and *TRACE* images. To adjust the co-alignment between the MDI and SOT images we used the sunspots observed in the Hα images. The co-alignment between the EIS and *TRACE* data sets was also checked by matching the bright features observed in the wider context images taken by EIS (Si X) and the *TRACE* 171 Å images. We estimated the uncertainty of our final co-alignments to be at most 5″−10″.

3. Ejection of filament material and near-concurrent small flare observed with *Hinode*/SOT Hα

Figure 2 gives an overview of the erupting region, showing SOT Hα images of the observed region with an MDI magnetogram superimposed. In the portion of the region shown here, there is a large positive patch, containing at least two spots on its western side, and this is surrounded by a negative region. Thus there is a PIL that surrounds the positive polarity region, but this inversion line is most prominent in the west (between the sunspots), and in the northwest and to the southeast, and much of the activity we see occurs mainly along these three portions of the inversion line; we identify these locations as the northwest, west, and southeast PILs in Fig. 3b for future reference. (The above-defined 4 UT brightening occurs along the northwest PIL.) The filament had an S shape, which was observed in absorption in Hα sitting along the PIL.

A strong brightening (black arrow in Fig. 2a) appeared north and slightly east of the sunspots, on the northwest PIL, in the first SOT image taken at 04:00 UT (Fig. 2a). An "intruding" positive polarity was observed in the negative-polarity region, also near the northwest PIL. Between 5:00 and 5:30 UT, an ejection is observed in the SOT images, with some filament material appearing to slide out towards the south (equivalent to the "fast-rise" phase of the eruption). Flare ribbons were observed in the Hα images between 05:12−05:44 UT, close to the intruding positive polarity (Fig. 2b). Even earlier there are hints of ribbons in the northwest, and also in the southeast, specifically between about 04:30 and 05:00 UT. From about 05:20 UT other ribbons appear south of the spots along the west PIL, and ribbons become prominent along the southeast PIL at this time. Thus, several locations along the PIL erupt. It is not simple to say which ribbons started first, but it is from the northwest PIL that the violent filament eruption emanates, and it is the ribbons that occur along the west PIL that correspond to the brightest flare in soft X-rays (SXRs) at the time of peak *GOES* intensity (cf. Sect. 6). It appears that the filament did not erupt completely, but rather the eruption was partial, because much of the filament could still be seen on the disk after this event.

4. EUV *TRACE* and *STEREO* observations of the eruption

We obtained quality data of the eruption in EUV from both *TRACE* and *STEREO*. As the information derived from the two spacecraft is similar, we present the results for one of them, *TRACE*, in most detail. Figure 3 shows four *TRACE* 171 Å images from prior to and during the eruption, overlaid with magnetograms from MDI. These frames are from the corresponding video 1, which shows the entire eruption sequence.

Figures 3a and 3b are prior to the onset of the main eruption. They show that large-scale loops in the region expand over this period, with two of the loops pointed out by arrows in panels a and b. Examining low-cadence EUV images from *STEREO* shows that this loop expansion started near 23 UT on

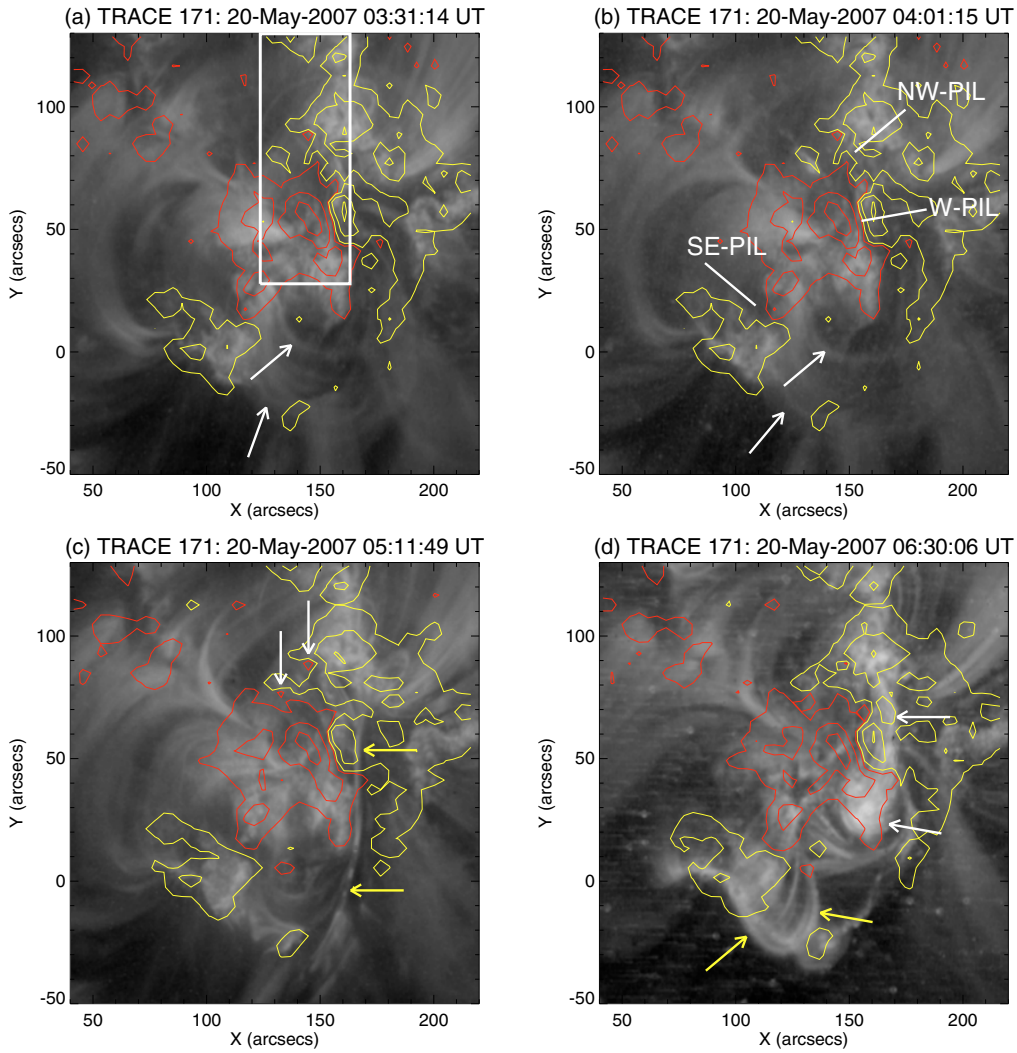

Fig. 3. Frames from video 1, showing *TRACE* 171 Å images of the erupting filament region with *SoHO*/MDI contours superimposed. Red and yellow (switched from blue in this figure for clarity) contours are respectively the positive and negative polarities from an MDI magnetogram taken at 03:15 UT in **a)** and **b)**, 04:51 UT in **c)**, and 06:23 UT in **d)**, all on 2007 May 20, with contour intensity levels the same as in Fig. 2. Indicated by arrows in **a)** are two loops, which expand outward by the time of **b)** during the period prior to the main filament eruption. In **c)** the white arrows are locations where repeated brightenings occur at the base of the jet-like erupting prominence, with the eastern arrow near the site of the the EUV counterpart of 4 UT brightening of Fig. 2 on part of the polarity inversion line (visible from ~03:57 UT in the video) and the western arrow near the site of the EUV-brightening counterpart of the ribbon pointed out in Fig. 2 (visible from approximately 04:01 UT). Yellow arrows in **c)** show the erupting filament. In **d)**, white and yellow arrows respectively point out two sets of post-flare arcades, with the arcade of the white arrows traversing the west side of the active region's polarity inversion line, and the arcade of the yellow arrows traversing the southeast portion of the polarity inversion line. The rectangular box in **a)** shows the field of view (FOV) of the EIS instrument. Labels in **b)** show the southeast, west, and northwest portions of the polarity inversion line, the full extent of which surrounds the large positive region. The video is available in the electronic edition of the article.

2007 May 19, and these loops open up during the eruption. The speed of these expanding loops is ~1−2 km s^{-1}; Uchida et al. (1992) found X-ray active region loops to expand at "a few to a few tens" km s^{-1}, and considering possible projection effects our measured velocities of these EUV loops fit in the lower end of that range. Figure 3c shows the eruption in progress, with the prominence erupting in the form of a jet-like surge hugging the west PIL as it flows to the south. It is clear from the video that the surge originates in the northern part of the region, around and including the location of the white arrows in Fig. 3c. One of these arrows is where an intruding positive polarity is canceling with negative flux over the course of the eruption (with the positive flux decreasing in area between MDI magnetograms of Figs. 3c and 3d), while the other location is at a boundary between a clump of positive and nearby negative flux.

Frequently, active region filaments are observed to rise slowly for ~10−30 min before their CME-producing fast rise (Kahler et al. 1988; Sterling & Moore 2005; Chifor et al. 2006), which can be part of the activation process as discussed in Sect. 1. Since we observed the filament on disk, it was difficult to track any such slow rise that may have occurred here. We have, however, identified that pre-flare motions of the filament started from, at the latest, 04:42 UT in *TRACE* images, with the fast eruption starting near 05:11 UT, and so the duration of the slow motions is consistent with the durations of filament slow rise phases, and we will refer to the early motions here as slow rise

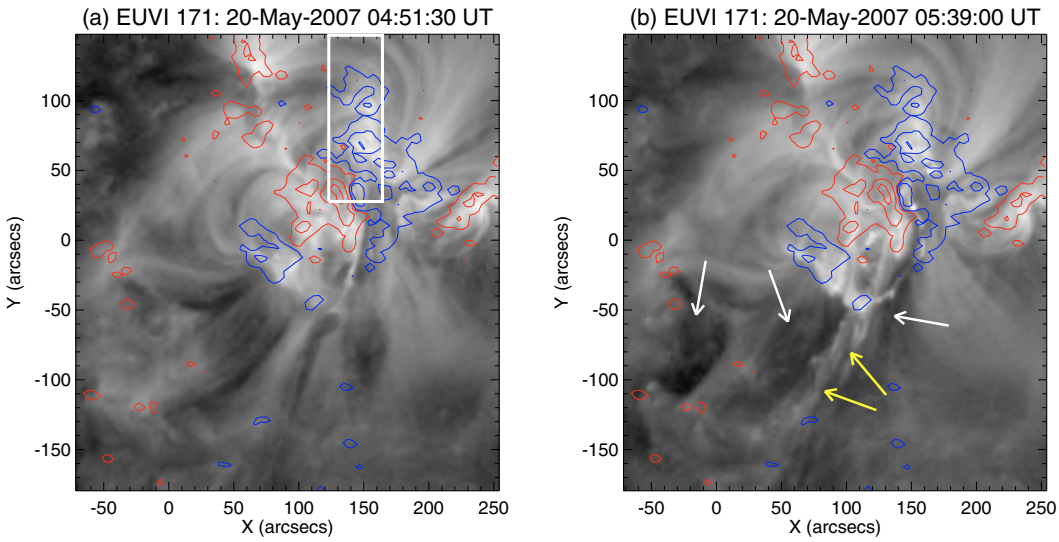

Fig. 4. *STEREO*-A/SECCHI/EUVI 171 Å images of the erupting filament region, with **a)** from prior to the eruption and **b)** from during the eruption. Yellow arrows in **b)** show the jet-like erupting filament, and white arrows show regions where coronal intensity "dimming" has occurred since the time of **a)**, as coronal material was expelled during the eruption. Red and blue contours are MDI magnetograms, as in Fig. 3, from 04:51 UT in both panels. Alignment with the MDI magnetogram is more crude with these *STEREO* images than with the images from *TRACE*, *Hinode*, or *SOHO*, because of the angular separation between *STEREO* and the Sun-Earth line. The rectangular box in **a)** shows the EIS FOV.

phase motions. (There may be an earlier phase to the eruption also, one which results in the loop expansion discussed above and in Fig. 1; this is a topic for future consideration.)

Based on video 1, we can present a chronology of the pre-eruption and eruption phase:

- Large-scale EUV loops expand at ~1−2 km s^{-1}, from ~23:00 UT on May 19.
- From the start of the video at 03:22:16 UT (presumably continuing from earlier times), there are repeated transient EUV brightenings in the region's north.
- From ~03:57 UT the EUV counterpart of the SOT 4 UT brightening in Fig. 2 appeared on the northwest PIL, at the location of the eastern white arrow in Fig. 3c, and there are transient brightening episodes at about the same location at both earlier and later times.
- Between 04:46:24 UT and 04:52:56 UT, there is brightening near the site of the intruding polarity, about 15″ west of where the 4 UT brightening occurred.
- From ~04:45 UT, surge-like motions become apparent, with intensity brightenings and flows apparent running southward along the main PIL. The base of the ejecting surge is rooted in the region's north near the intruding polarity.
- From ~04:55 UT, onset of detectable SXR emission in the *GOES* data (Fig. 1).
- From ~05:07 UT, there is another brightening at the same location as the 04:46:24 UT brightenings.
- Between ~05:07 UT and 05:12 UT, the jet becomes prominently visible, outflowing from that brightening location (the jet's base); the yellow arrows in Fig. 3c point to this outflowing jet/surge. This five-minute period appears to be the onset of the main phase of the eruption of the jet, that is, the onset of the eruption's "fast phase", and this time corresponds to within a few minutes to the time of a positive gradient in the *GOES* light profile in Fig. 1. (Sterling & Moore 2005, present in their Fig. 3 another example of a similar relationship between the rise speed of a filament and various intensity profiles.) During this eruption, the filament jet is rooted very near the ribbon pointed out in Fig. 2b, as can be seen in the video from ~05:09:43 UT.

Figure 3d is from late in the eruption sequence, after the jet has been ejected. White and yellow arrows in the figure respectively show two different sets of post-flare loops. Both sets of loops sit over respective PILs, with the northwest and west set of loops over the PILs in the west, along which the jet was ejected. The eruption of the prominence resulted directly in the formation of those loops in the west, and apparently the loops in the southeast resulted from destabilization and eruption of the field along the southeast PIL.

The eruption has effects on the corona further afield, as evidenced by strong intensity dimmings that are well seen in the *STEREO*/SECCHI/EUVI images. Figure 4 shows an example, with large areas in the south dimmed after the filament eruption is well underway. The eruption removes magnetic loops to the south, resulting in the density-evacuated regions and the consequent dimmings. Inspection of EUVI 284 Å images indicate that activity in the region that dimmed began by at least 04:20 UT, but with the strongest dimmings beginning between 05:00 UT and 05:20 UT. Thus, an eruption whose initial flare nucleus was in a rather confined region of a few tens of arcsec, involved a large-scale eruption covering at least 200″. Moreover, inspection of the full-frame EUVI images show that weaker dimmings grow to cover an even larger extent than shown here. This sort of large-scale eruption with a more localized flaring region has now been detailed for several cases (e.g., Gopalswamy & Thompson 2000; Wang et al. 2002; Sterling & Moore 2004; Attrill et al. 2008; Moore & Sterling 2007).

5. Evolution of the magnetic field in *SoHO*/MDI magnetograms

In a movie constructed from the magnetograms of the active region and surrounding area, it appears as if the two main positive and negative areas of the active region, including the sunspots between which the filament was located, were approaching each

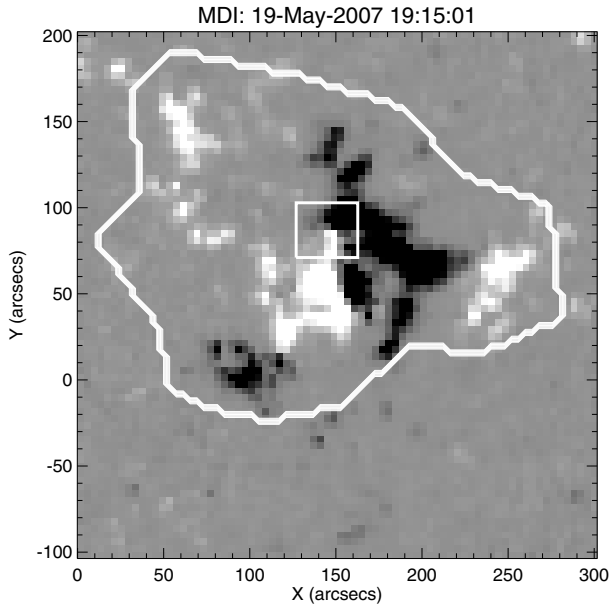

Fig. 5. Active region in which the 20 May 2007 flare occurred. The irregular contour outlines the area over which the fluxes of the region were computed in Fig. 6. Inner rectangular box shows region over which fluxes from MMF-like elements were considered.

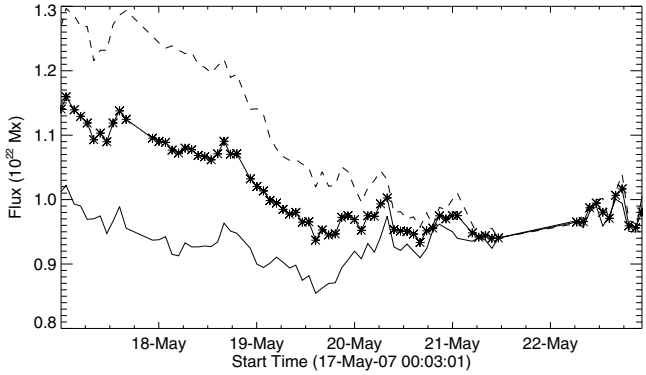

Fig. 6. Fluxes as functions of time computed from the area inside the irregular contour of Fig. 5, where the solid (dashed) curve is the positive (unsigned negative) flux. The stared solid-line curve is the total unsigned flux multiplied by 0.5, giving an estimate for the total unsigned flux for the region.

other from at least 18 May, two days before the eruption. To investigate this, we analyzed the magnetic flux from MDI 96-min cadence magnetograms of the region for evidence of magnetic cancelation occurring during this period.

There are a number of intrinsic complications to measuring magnetic flux over several-day periods from instruments such as MDI. For our analysis we have essentially followed the method described in some detail by Green et al. (2003) of selecting out visually a contour that contains almost all of the obvious flux of the active region, for the entire period of relevance to our studies. Figure 5 shows the primary contour we settled on for this analysis; we considered several others, but the general evolution of the flux measurements were not strongly dependent on this selection as long as the main flux elements were enclosed. An advantage of isolating the region in this fashion is that it avoids much of the noise in the non-active region Sun, which in some circumstances can add up to a disruptive fraction of the total flux; this noise is both from background fields not belonging to the active region itself, and from uncertainties in the magnetograms themselves (discussed below). We applied standard considerations to the analysis, such as accounting for the $(\cos\theta)^{-1}$ reduction in the line-of-sight component of the flux for fields away from disk center, where we work under the assumption that all fields are normal to the solar surface. Similarly, we also account for the apparent change in surface area of the region due to foreshortening when it is away from disk center.

Uncertainty in the flux densities in each pixel are 20 G for un-summed MDI magnetograms (Scherrer et al. 1995). Some of the magnetograms are sums of five shorter-duration magnetograms, in which case the uncertainty is 9 G (Green et al. 2003). For our data set, MDI alternated between modes of summed and non-summed magnetograms, and so there are a mixture of uncertainties in the resulting values. By using the contour of Fig. 5, we reduce the contribution of this noise by avoiding inclusion of quiet-Sun fields, many of which are near the noise limit. We used the same contour for the entire period of our analysis; using a new contour at each time step would reduce the uncertainty in our results somewhat, but we did view a movie of the flux contained within the selected contour and visually verified that regions of substantial flux do not enter or exit that contour.

We also checked the data for pixels indicating a substantial degree of saturation, or "corrupted pixels", in the Green et al. terminology, by searching for pixels that show both weak continuum intensity (indicative of sunspots) and apparent low magnetic field strength, again following Green et al. From MDI synoptic data from when AR 10956 crossed central meridian on 2007 May 19, we found nine pixels (out of over 4000) that were corrupted, with all of them being positive flux. These would result in an underestimate of our derived positive fluxes of a few percent at most. As these values were only a "snapshot", derived from only one time, the number of partially-saturated pixels at other times may have varied somewhat, but in any case we do not expect this to have a substantial effect on our total derived flux intensities.

Green et al. (2003) discuss a calibration factor for MDI data they used of 1.45 for weak and moderately strong fields, and of 1.9 for stronger fields, based on results from Berger & Lites (2003). Since late 2007 however, all of the MDI magnetograms have been recalibrated (increased by a factor of about two; Hoeksema 2007, private communication, and the MDI webpage) over the older values available at the time of those earlier studies. Therefore we did not apply any multiplicative factor to our magnetograms, which are all of the recalibrated variety.

Figure 6 shows our resulting integrated magnetic flux values as functions of time. For much of the period the fluxes are not in balance, with negative flux dominating the positive flux. This imbalance decreases with time, and the two fluxes become roughly equal from around May 21. Intuitively one might expect the two fluxes to be in balance, if the enclosed flux is all part of the same closed flux system. It turns out, however, that flux imbalance is very common. Green et al. (2003) explored this phenomenon in detail, and determined that such an apparent flux imbalance can result from geometrical effects of measuring line-of-sight fields on the spherical solar surface. For east-west-oriented active regions, they found that the following polarity dominates when regions are in the east and the leading polarity dominates when regions are in the west, with the two polarities matching only around the time of central-meridian passage; this is consistent with those regions being composed of a system of basically east-west-oriented loops. Of most interest to our study here regarding these long-term flux evolutions is that prior to late on May 19, both the negative and positive fluxes are decreasing with time,

and hence the total unsigned flux is decreasing over this period (the above-mentioned loop-geometry effect would lead to the apparent decrease in flux of one particular polarity, and a concurrent increase in flux of the other polarity). This supports our suspicion that there is flux cancelation occurring between the positive and negative regions of the active region, at least to within a few hours of the time of the eruption on May 20.

In comparing our result in Fig. 6 with the Green et al. considerations, our approximate flux equality near May 21 is reasonably consistent with their suggestion of near equality of fluxes at the time of central meridian passage, which occurred on May 19. Prior to this near-equality however, our findings appear to be in conflict with the arguments of Green et al. Figure 5 shows our following polarity is positive, and so according to Green et al., it would be expected that the positive polarity would dominate prior to the fluxes reaching equality on May 21, but from Fig. 6, the opposite is the case. It is possible that our results differ from the Green et al. expectations because our selected contour does not well-enough isolate the flux of the independent active region. We have tried using a different contour, smaller than that of Fig. 5 and which seems to isolate better the main positive and negative regions of the active region. Nonetheless, the polarity-dominance ordering with time remains the same as in Fig. 5. We have verified that our code does reproduce the polarity-dominance orderings found by Green et al. (2003) for the four specific regions that they examined, and so the question of why the polarity-dominance ordering for our region differs from the Green et al. findings remains unresolved. Possibilities include that our region is too complex to interpret in a simple bipolar approximation, as if viewing a simple east-west-oriented loop at various longitudes. Another possibility is that our positive flux is underestimated enough due to saturation to account for the discrepancy. Despite these questions, we can state that our observations are consistent with a decrease in total unsigned flux of the active region with time (at least until around 12 UT on May 19), and this in turn is consistent with continuous magnetic cancelation occurring between the approaching flux polarities. This apparent flux decrease occurs over several days prior to the May 20 eruption along the main PIL of the region. This is consistent with the cancelation disrupting the stability of the region, preparing it to be triggered to eruption.

We can estimate the amount of flux canceled as the two flux polarities approach each other. From Fig. 6, over the 24 h from 12 UT May 18 until 12 UT May 19, the total flux drops by $\approx 1 \times 10^{21}$ Mx (recalling that the total active region flux is 0.5*(positive flux + |negative flux|), assuming that both ends of all the active region's loops are enclosed within the integrated region). As the total flux in the region of the contour is $\sim 1 \times 10^{22}$ Mx, about ~10% of the flux cancels over that 24 h period. At later times (after about 12 UT on May 19), the negative and positive fluxes do not show clear trends, but by then the active region is clearly more complex than a simple east-west dipole, making it difficult to infer how the flux is actually changing with time (increasing, decreasing, or remaining level).

From 01:39 UT on May 20 we observed a new positive flux at coordinates (140, 80) in the MDI overlays shown in Fig. 2. We also observed negative flux canceling to the east of this new flux element, at approximate coordinates (130, 75) in Fig. 2, on the northwest PIL. At least some of the positive flux in this region appears to belong to a series of moving magnetic features (MMFs, Harvey & Harvey 1973), flowing from the positive spot in the south into the northern negative-polarity magnetic patch with velocity ~0.5–1.0 km s^{-1}. The location where this flux cancels in the northern negative-polarity patch corresponds to the 4 UT brightening of Fig. 2 at 03:57 UT on May 20. The coarseness of the MDI time cadence however makes it difficult to differentiate between true MMF elements and possible new emerging flux elements, therefore we will refer to them as "positive flux elements" in the following, for purposes of identification. We also expect that our "intruding polarity" in the northwest PIL region is one of these positive flux elements. Figure 7 shows an apparent cancelation of flux just prior to the time of the rapid filament eruption. The filament ejection started near where these positive flux elements cancel with negative field, near the flare ribbon location.

We have studied the behavior of the flux in the neighborhood of where the positive flux element cancelation takes place. Specifically, we have monitored the positive flux inside of the small box in Fig. 5. Several positive flux elements enter into this box, presumably flowing in from the south, and disappear before reaching another boundary of the box. We do not attempt to make a comprehensive study of the fluxes in this box, since over this small area inside of the active region there is much movement of substantial flux into and out of this area's boundary over time. We can, however, track the evolution of some of the positive flux elements by monitoring the positive flux only. We find that after positive flux enters the box, the measured positive flux in the box undergoes sharp drops in magnitude at times corresponding to when the magnetograms show positive flux to disappear, such as near 10 UT on May 19, and near 0 UT on May 20; the former of these results in a positive-flux drop of $\sim 1 \times 10^{20}$ Mx, and the second of these is $\sim 2 \times 10^{20}$ Mx. Due to the proximity to the onset of the filament ejection, we suggest that cancelation of these positive flux elements triggered the eruption, following the more-gradual cancelation of the larger-scale active region fields, discussed above, which brought the system to the brink of instability.

Several workers have found MMFs to play a role in eruptions. For example, Brooks et al. (2007) found MMF cancelation near the base of surges, and Zhang & Wang (2002) argue that continuous emergence of MMFs triggered a series of X-class flares in a region they studied. Deng et al. (2002) found MMFs cancelation involving $\sim 10^{19}$ Mx each to result in activation of, and ejection of material "blobs" onto, a filament they investigated; that filament, however, did not erupt. In our case, eruption likely occurred only because the system was already destabilized enough by the larger-scale field cancelation to result in easy disruption by our series of positive flux elements, which are likely to be MMFs or similar features.

6. Soft X-ray *Hinode*/XRT observations of the eruption

Pre-eruption brightenings (including one corresponding to the 4 UT brightening of Fig. 2) were also observed in the core region seen in *Hinode*/XRT images. Transient brightenings along the northwest PIL (and perhaps the west PIL) are underway from at least 4 UT on 2008 May 20, which is the earliest time we examined in SXRs. Moreover, the arcade along the southeast PIL shows activity (expansion) from at least as early as 04:16 UT; this could be a response to cancelation of positive flux elements occurring in the region north of the sunspots, perhaps earlier episodes of such cancelation than we have considered in Sect. 4.

A sigmoid (e.g., Rust & Kumar 1996; Sterling & Hudson 1997; Moore et al. 2001) was observed to form connecting the negative flux region northwest of the filament with the region south-east and east of the sunspots (Fig. 8). The sigmoid was

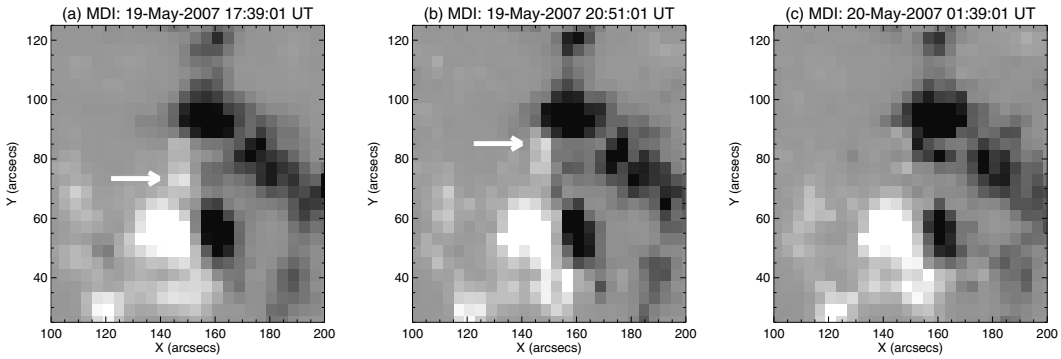

Fig. 7. MDI magnetogram sequence (closeups of Fig. 5) showing (**a)** and **b)**) a positive-flux magnetic feature, which we refer to as a "positive flux element", but which could be a moving magnetic feature (MMF), appearing to flow from a positive sunspot into toward the a patch of negative flux in the north. In **c)** the positive-flux feature has largely disappeared, apparently having canceled with the patch of negative flux. The cancelation site is near the location where the filament eruption is rooted, suggesting that the flux cancelation played an important role in the onset of the eruption.

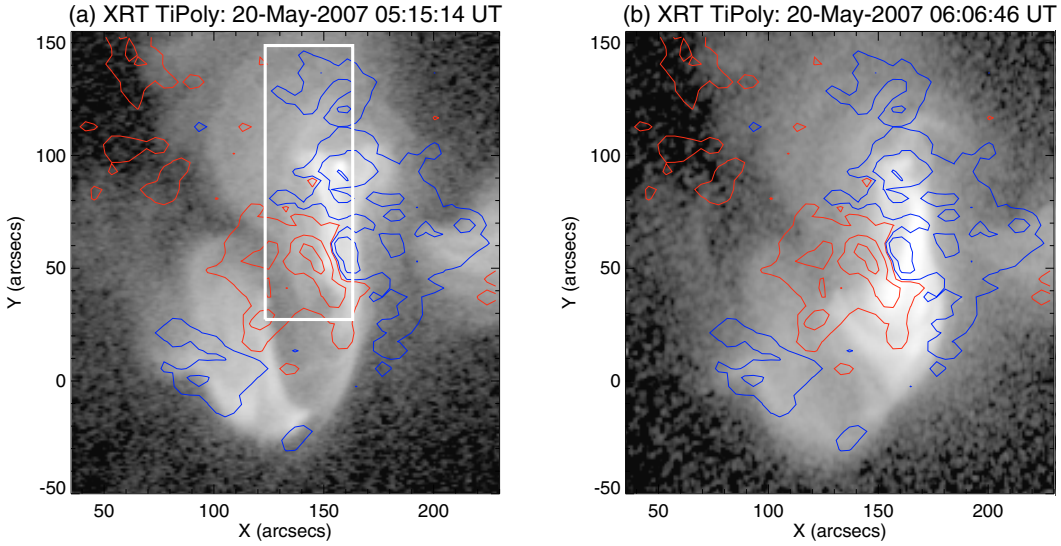

Fig. 8. *Hinode*/XRT Ti_poly images of the erupting region **a)** near the time of onset of the rapid filament eruption, and **b)** near the time of the peak in *GOES* SXR intensity. Overlaid on the image is an MDI magnetogram taken at 04:51 UT on May 20. Red and blue contours are respectively the positive and negative polarities, with contour levels the same as in Figs. 2 and 4. The rectangular box in **a)** shows the EIS FOV.

clearly visible starting at 04:58 UT, and thus it forms late in the "slow-rise" phase of the filaments ejection, and continues its evolution at the start of the fast-rise phase; this is similar to sigmoids observed forming and rapidly evolving during the slow-rise phase in studies of Sterling et al. (2007a,b). Early during the eruption (Fig. 8a), the flaring loops corresponding to the two arcades seen in the EUV images are illuminated, that is, one along the west PIL, and one in the east along the southeast PIL; the sigmoid forms when brightenings in the south link the two arcades, likely along the fainter portions of the PIL. Later, near the time of the peak of the eruption in *GOES* SXRs (Fig. 1), the loops along the western PIL dominates the SXR intensity in the XRT image (Fig. 8b).

7. *Hinode*/EIS observations of the eruption onset region

The fast-cadence EIS data sets obtained between 00:59–05:15 UT covered an area of the active region that included the eruption onset region and northern magnetic cancelation site. Figures 3a, 4a, and 8a show the EIS FOV of the fast-cadence data sets overlaid onto *TRACE*, *STEREO*/SECCHI/EUVI, and XRT images, respectively, along with the MDI magnetogram contours in each figure. A brightening corresponding to that indicated by the black arrow in Fig. 2a was visible in the EIS raster data sets obtained between 03:57–04:01 UT, in coronal lines as well as transition region lines, in the range of temperatures Log T_e = 4.8–6.3. We did not observe small-scale transient brightenings at flare temperatures (e.g. in the EIS Fe XXIII line).

Figure 9 shows EIS images taken in the Fe VIII and Fe XII line emissions as well as corresponding Doppler-shift and line FWHM measured from the Fe XII observations. When measuring the relative Doppler velocities, we assumed that the Fe XII reference wavelength is equal to the average center of lines fitted within each raster. A more accurate reference wavelength would be obtained by averaging the fitted Fe XII line centers in a quieter region of each raster; this was possible in the case of the context raster of wider FOV, but the fast rasters were too small to identify such a region.

Several prominent preflare brightenings that appear at the base of the ejected filament observed by *TRACE* and SECCHI/EUVI were also clearly observed by EIS. Other transient brightenings were observed in the EIS data sets

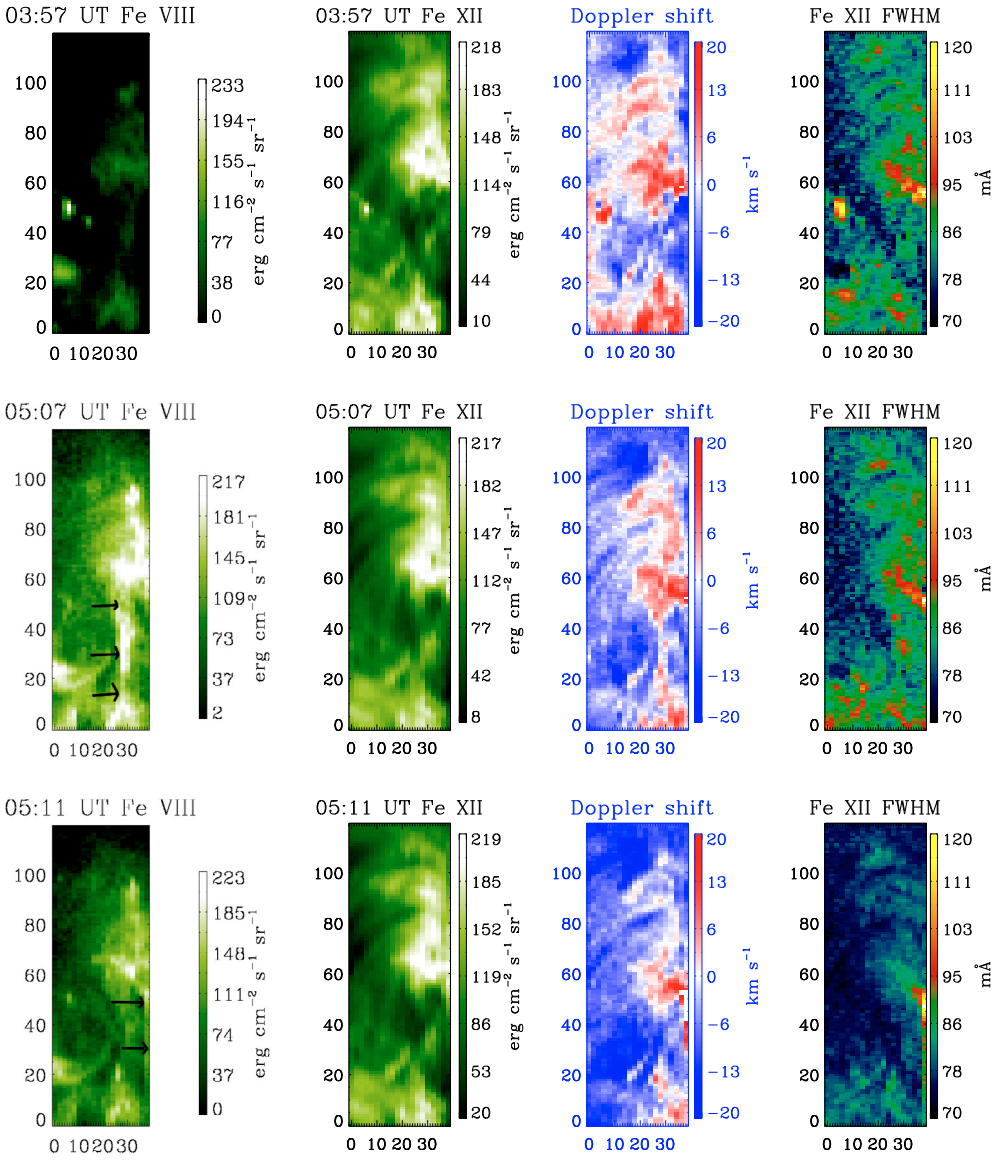

Fig. 9. EIS Fe VIII and Fe XII intensity maps, Fe XII Doppler-shifts and line FWHM. Several brightenings are apparent in the intensity maps around the filament's base location, particularly in Fe VIII (cf. Fig. 3). Arrows on the Fe VIII images indicate a feature that likely corresponds the the erupting filament seen in the TRACE images (see text). Persistent line broadening and relative red shifts occurred in the observed region. In these panels, and in the panels of Fig. 11, the *X* and *Y* coordinates give the relative distances in arcseconds inside the EIS raster FOV, rather than relative to Sun center as in other figures.

beginning at 03:45 UT and 05:07 UT (particularly in Fe VIII). Figure 10 shows the Fe XII intensity, Doppler shifts and line FWHM obtained from the fast raster data sets obtained from 03:57 UT (prior to the filament slow-rise) with MDI contours superimposed. Some of the prominent intensity enhancement in the EIS data sets (e.g., the 05:07 UT Fe VIII image in Fig. 9) are located along the PIL in the west (also compare with Fig. 9, top row).

We observed persistent relative red-shifts and line broadening (Fe XII) along the west PIL and in the vicinity of the positive flux element intruding polarity location (northwest PIL). Transient brightenings, including one corresponding to the 4 UT brightening of Fig. 2, appear co-located with a strong red-shift component and an indication of a blue-shifted component along with strong nonthermal line broadening (Fig. 10).

A counterpart of the sudden brightenings observed in the broadband (*TRACE* and *STEREO*) EUV images that marked the onset of the filament eruption's fast-rise (Sect. 4, and white arrows in Fig. 3c) was also observed by EIS, in at least the Fe VIII line. In the 05:07 UT scan it appears as a linear feature with a bright base (arrows in 05:07 Fe VIII scan of Fig. 9), and this linear feature roughly coincides with the filament being ejected in the *TRACE* movie (video 1) at about the location of the EIS FOV (cf. Fig. 3a). As is evident in that video, the filament has a brightening on the NW-PIL at 05:07 UT in *TRACE*, and that coincides with the EIS 05:07 UT raster feature to within the accuracy of our alignment. At 05:11 UT in the video 1 *TRACE* movie, a different strand of the filament is most prominent, located about 10″ west of the 05:07 UT *TRACE* brightening. This 05:11 UT *TRACE* filament strand may also be visible at the western edge of the EIS FOV (arrows in in 05:11 Fe VIII scan of Fig. 9), but this is part speculation because most of the putative feature is not inside the EIS FOV. Thus we suspect that we are observing in the EIS data a part of the filament at the time of eruption in at least the the Fe VIII raster at 05:07, and perhaps at 05:11 UT also.

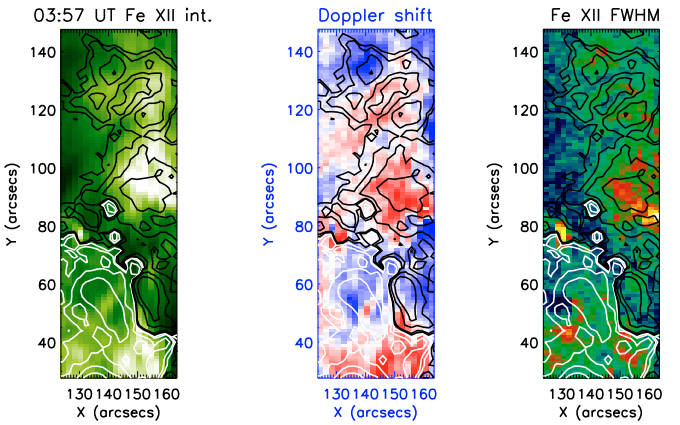

Fig. 10. Fe XII intensity, Doppler-shifts and line FWHM obtained from the raster data sets beginning at 03:57 UT prior to the filament slow-rise. MDI contours of the magnetogram taken at 04:51 UT are superimposed: white represents the positive polarity, while black represents the negative polarity. Contours are 25, 70, 300 and 850 G. Red-shifted flows and line broadening were observed along the west PIL and in the vicinity of the intruding positive polarity region (northwest PIL).

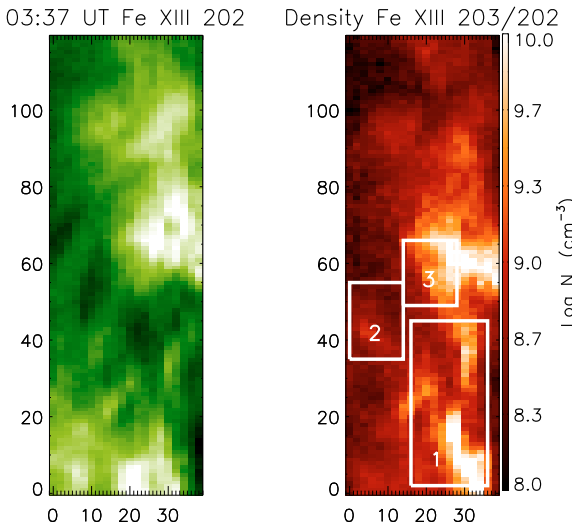

Fig. 11. Fe XIII 202 intensity image and density map derived from the Fe XIII 203/202 diagnostics. The boxes indicated in the density image at 03:57 UT represent: 1 = the west PIL; 2 = northwest PIL region (corresponding to the location of the 4 UT brightening of Fig. 2); 3 = intruding positive polarity region (positive flux element cancelation region). For each of these regions we measured the density changes shown in Fig. 12.

We obtained electron density values for the onset region of the eruption using density sensitive line pairs observed with the "CAM_ARTB_RHESSI" EIS sequence and theoretical line intensity ratios calculated with CHIANTI v.5.2 (Dere et al. 1997; Landi et al. 2006). The Fe XIII λ203 line is blended with a Fe XII line, which we removed by fitting a double Gaussian. The Fe XIV λ274 and the Mg VII λ278 lines are each blended with a Si VII line. To remove this blend, we used another, relatively strong, Si VII λ275 line. Young et al. (2007a,b) give details on using these density diagnostic lines. Because there is an error in one of the Fe XIII atomic data files in CHIANTI v.5.2, we used a corrected file for the present analysis, which will be made available in the next CHIANTI database release. Young et al. (2009) provide a thorough overview of data analysis issues for the best density diagnostics of Fe XIII.

Figure 11 shows an Fe XIII 202 Å intensity image and density map derived from the Fe XIII 203/202 diagnostics. The boxes indicated in Fig. 11 represent the regions of interest where we measured density changes: 1 = west PIL; 2 = northwest PIL region, where the 4 UT brightening noted in Fig. 2 occurred; and 3 = the intruding positive polarity region (i.e., the positive flux element cancelation region).

Figure 12 shows the evolution with time of the average density in these regions measured from the Mg VII (Log T_e = 5.8), Fe XIII (Log T_e = 6.2) and Fe XIV (Log T_e = 6.3) diagnostics, and Table 2 summarizes the results. For some of the lines and locations, there is a sharp peak in the density near 04:00 UT, each of duration of a few minutes; the basic values shown in the table, Cols. 2, 4, and 6, are the densities averaged over time and over the area of the boxes outside the time of these strong density spikes, while the "Spike" values, Cols. 3, 5, and 7, give the measured density values averaged over the boxes, but only at the times of the occurrence of those density spikes.

In each of the three regions, the measured non-spike density values decrease with temperature; thus the coolest material (in the considered temperature range) is most dense in the three regions. Uncertainties listed in the table indicate the range of scatter in the non-spike density values over 01:00 UT to 05:30 UT on 2007 May 20.

The density spikes occur first in the Box 1 region, i.e. the western PIL, at ~03:45 UT. About 12 min later (in the raster starting at 03:57 UT), a spike in density occurs in Box 2, the northwest PIL region. We see the spike in both the Fe XIII and the Fe XIV diagnostics in both regions. Although the filament erupted along the western PIL region (near or through Box 1), the density spike is ~1 h prior to the obvious filament eruption. Box 2 corresponds to the location of 4 UT brightening of Fig. 2 however, and, as discussed in Sect. 4, from ~03:57 UT, that location brightened in EUV, and this is possibly a cause or consequence of the triggering of the eruption. Therefore, currently all we can say is that the trigger process seems to have been connected with a transient increase in density in the eruption region for this event. Whether this connection is significant will be determined by whether similar pre-eruption density enhancements are observed in future studies of other events.

8. Discussion

We observed a partial filament eruption occurring in an active region and accompanied with a *GOES* class B6.7 small flare and a CME. A converging motion between opposite-polarity sunspots resulted in cancelation of field for some days around the primary magnetic neutral line (west PIL), along which filament material was located before eruption. The source location of the eruption was a negative-polarity magnetic region located north of the interacting sunspots. The eruption occurred near a new positive flux element (which we also refer to as an intruding positive polarity in the the negative field region, and which may be an MMF) that may have triggered the slow-rise motion of the filament, and the filament's subsequent CME-producing ("fast-rise") ejection.

We found persistent red-shifted bulk-flows (in the Fe XII emission), and nonthermal line-broadening along the PIL. Small-scale transient brightenings were observed in the filament core prior to eruption at both transition region and coronal temperatures. These brightenings were located near the base of the ejected filament, and along the west PIL. We found abrupt, localized density enhancements measured at coronal temperatures

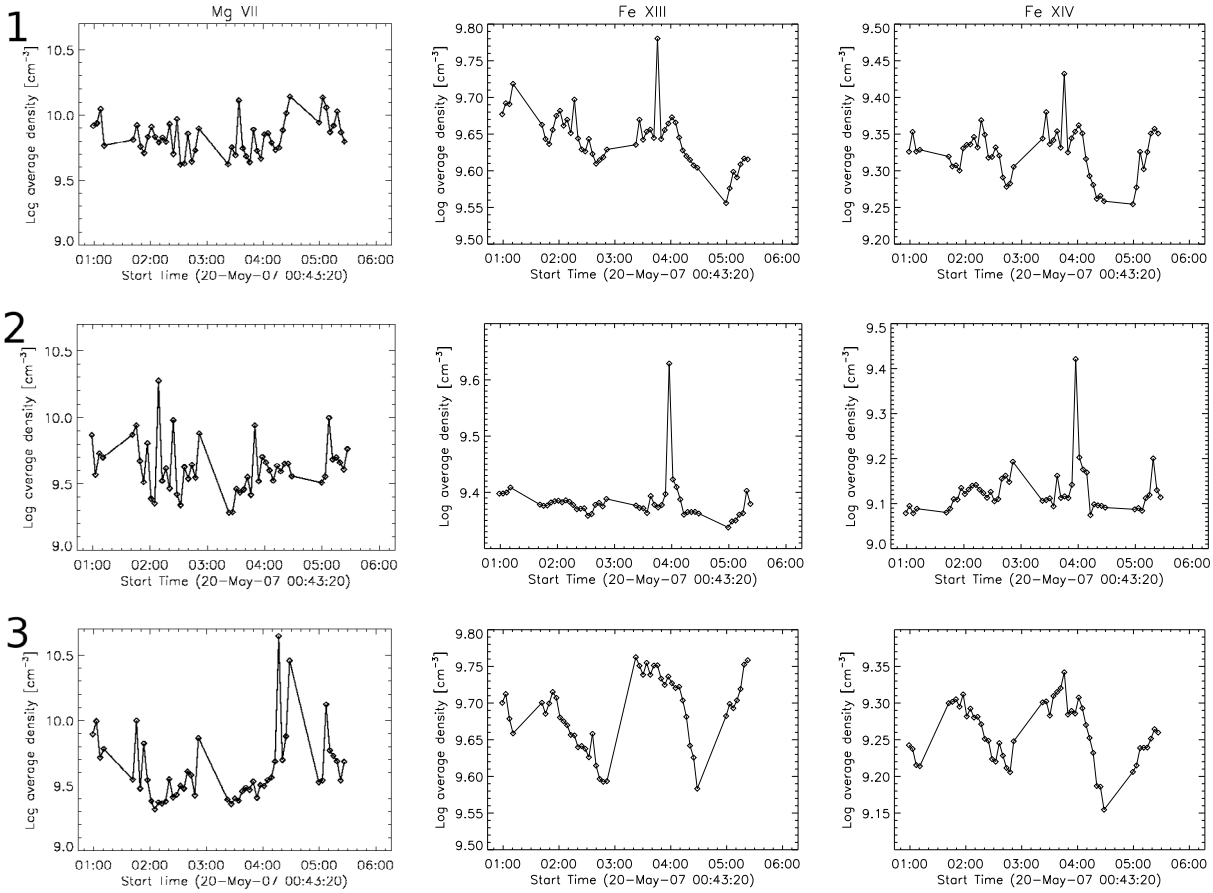

Fig. 12. Evolution of the density measured from the Mg VII (left column), the Fe XIII (middle column) and the Fe XIV (right column) diagnostics in the main polarity inversion line region (*top*), in the north-east part of the polarity inversion line (corresponding to the 4 UT brightening of Fig. 2) region (middle), and in the emerging flux region (*bottom*). These regions are indicated in the density image at 03:57 UT in Fig. 11 (1 = main polarity inversion line, 2 = north-east inversion line, 3 = emerging flux region). A strong spike in density occurs near 4 UT in regions 1 and 2 in the Fe XIII and Fe XIV channels.

Table 2. Log averaged densities (cm^{-3}) over box locations within eruption region.

Location	Mg VII	Mg VII Spike	Fe XIII	Fe XIII Spike	Fe XIV	Fe XIV Spike
Box 1	9.9 ± 0.3	No*	9.65 ± 0.10	9.78	9.31 ± 0.06	9.43
Box 2	9.7 ± 0.5	No	9.37 ± 0.05	9.63	9.13 ± 0.07	9.42
Box 3	9.8 ± 0.6	No?	9.68 ± 0.08	No	9.25 ± 0.10	No

Notes. Columns 2, 4, and 6 are densities averaged over boxes of Fig. 11, and over time outside of enhanced density ("spike") times. Columns 3, 5, and 7 are densities averaged over boxes of Fig. 11 during times of enhanced-density spikes.
(*) "No" means no spike apparent within the scatter of the data.

(Log T_e = 6.2−6.3), along the PIL during the pre-eruption period. The averaged density outside the time of these enhancements measured in the onset region decreased with temperature.

The surge-like filament motion began prior to the main flare onset. Martin (1989) describes three types of activations initiated near flare times, often within one hour of the onset of the main flare loops: (1) preflare activation and eruption; (2) surge-like activation; and (3) activation via impact from ejected mass or shock wave produced by a neighboring flare. For our case under study here, Martin's second type of activation is certainly occurring. (It is also possible that this may be an aspect of the first type of Martin activation also.) As the base of the surging filament was where the flux cancelation occurred, our observations are consistent with the cancelation being important for both the filament activation and the subsequent main eruption. This is consistent with other findings that flux cancelation can cause filament activation in at least some cases (e.g., Deng et al. 2002).

An SXR sigmoid was observed to form connecting the negative flux region northwest of the filament with the region southeast of the sunspots, during the late period of the filament's slow-rise phase and at the start of the fast ejection ("fast-rise phase"). That fast-rise phase of the eruption was marked by a surge/jet ejection of material observed in EUV and Hα, and its start was accompanied by a sharp increase in the SXR intensity. The SXR images also show dynamic changes in the region and surrounding corona from at least an hour prior to the eruption. This could be due to earlier episodes of positive flux elements canceling with surrounding field, or it could indicate that even more complex processes than we consider here are at work (e.g., a close synergy between the cancelation of the sunspots along

the west PIL, and the positive positive flux elements canceling with the negative field in the north).

Our observations provide strong evidence that the source of the filament ejection was where the localized positive flux elements were apparently interacting with surrounding negative field. Brightenings in the region in EUV at the time of the filament's fast eruption are consistent with the positive flux elements reconnecting with surrounding field, leading to the eruption. After the eruption starts in this location, the filament rapidly ejects along the region's west PIL, and flare loops develop along this west PIL. Nearby fields take part in the eruption, becoming destabilized along the west and southeast PILs. Regions further to the south, well outside of the active region where the filament eruption took place, are also involved in the eruption, likely due to the removal of remote field lines. This results in strong intensity dimmings to the south of the region that are well seen in EUVI images.

It has been found before that brightenings of transition region lines appear to be correlated to new magnetic flux emergence (Young & Mason 1997). Young et al. (2009) studied a small active region brightening observed in both transition region and coronal lines (Log T_e = 5.5−6.3). From the Mg VII diagnostics they found a density of 4×10^{10} cm^{-3}. This value has the same order of magnitude as the density measured in the onset region of the eruption analyzed here, where positive flux elements similar to MMFs have entered into a sea of negative field at the base of the erupting filament; so here the triggering agent would be the positive flux elements in a surrounding opposite-polarity region, which may have been MMFs rather than emerging flux.

Several eruption models involve emerging flux (e.g., Forbes & Isenberg 1991; Chen & Shibata 2000; Lin et al. 2001). Sterling et al. (2007a) found evidence for emerging flux triggering a solar filament's slow-rise. From their observations, Chifor et al. (2006) suggested that *localized* reconnection, which may have been triggered by emerging flux, may lead to the destabilization of an entire active region filament. Our analyzed event appears consistent with the positive flux elements playing a role similar to the modeled emerging flux, whereby it interacts with surrounding field and triggers the filament's slow, pre-flare motions, and eventually leads to the CME-producing fast ejection of filament material. Although our work here does not examine details of processes involved in causing the eruption, reconnection of field lines is strongly suggested by the presence and subsequent disappearance of the intruding positive flux element in the surrounding opposite-polarity region.

We can now return to the discussion of Sect. 1 of more general models for releasing energy stored in magnetic fields, in terms of the event discussed here. As mentioned in Sect. 1, often it can be difficult to determine which mechanism among several candidates is ultimately most responsible for fast-eruption onset. In the event studied here, we have presented evidence for tether-cutting flux cancelation being a trigger. Again however it is difficult to say that this mechanism alone is the cause. The converging spot fields could be responsible for the general expansion of the region, e.g., as evidenced by Fig. 3, and this expansion could be driving the system toward an ideal MHD instability independent of the apparent MMF-like cancelations. Nonetheless, the apparent cancelation of the MMF-like positive flux elements occurred very near the location where the filament jet originated, consistent with this flux cancellation being the trigger of the ensuing ejective eruption of the entire sheared-core arcade. Based only on the observations presented here, we cannot say whether such an eruption could have occurred with the convergence and cancelation of the spot flux alone or with the MMF-like flux cancelation alone. One way to determine the predominant triggering mechanism might be via numerical simulations mimicking the magnetic setup and pre-eruption flows that we observe.

Another potential method to gain insight into the likely main cause of this eruption is to observe and carefully analyze other eruptions occurring in a similar magnetic environment. An obvious eruption to consider is one that occurred in the same active region, but on the previous day, on 2007 May 19 starting near 12:00 UT. That event was analyzed by Li et al. (2008), Liewer et al. (2009) and Bone et al. (2009), while Veronig et al. (2008) focused on a coronal wave generated from that eruption. Alas however, those workers show that the May 19 event mainly occurred on a different PIL from the May 20 event of this paper, with the primary filament of the May 19 event located in the PIL west of that of the May 20 event (see in particular Bone et al. 2009). In Fig. 8, that May 19 PIL is between the red field at the extreme right edge of the panels, and the blue field just inside that edge. The full PIL can be seen in the images of Fig. 4 (at about (x, y) = (200, 30)). Thus a simple comparison between the two eruptions is not possible. Liewer et al. (2009) do state that heating events occurring during the onset phase of the May 19 eruption are "probably caused by flux cancelation occurrences", but a full detailed study would be required to say whether those events are really similar to what we see in the May 20 event.

Chifor et al. (2007) have shown that X-ray precursor brightenings to solar filament eruptions are situated close or near to the PIL, being associated with emerging and/or canceling magnetic flux. These observations were evidence for a tether-cutting mechanism initially manifested as localized magnetic reconnection being a trigger for the observed solar eruption. In the present paper, we observed the precursor activity across a wider temperature range, including Hα, EUV and SXR high-spatial resolution and cadence images as well as spectroscopic data from *Hinode*, *STEREO* and *TRACE*, and we measured the evolution of the magnetic field from *SoHO*/MDI images. The array of observations is consistent with the conclusions by Chifor et al. (2007) that precursor brightenings to filament eruptions are evidence of tether-cutting reconnection. Furthermore, from the present analysis, we were able to discuss the roles of large-scale magnetic flux cancelation (among the sunspots), and smaller scale cancelation (the positive flux element intruding polarity features): the pre-eruption sheared-core magnetic neighborhood was gradually destabilized by evolutionary tether-cutting flux cancelation that was driven by converging photospheric flows over several days. The persistent widespread flux cancelation along the main neutral line (west PIL) prior to eruption progressively "marched to the edge" the sheared-core active-region magnetic arcade. Then, localized magnetic flux cancelation(s) at the ejection site north of the main sunspots by the positive flux elements "kicked the sheared-core over the edge", triggering the ejection of filament material and CME.

Acknowledgements. We thank L. M. Green for useful discussions, D. Zarro for helpful software assistance, and T. Durgesh for assistance with graphics. We also thank an anonymous referee for helpful comments in an earlier version of this paper. *Hinode* is a Japanese mission developed and launched by ISAS/JAXA, collaborating with NAOJ as a domestic partner and NASA and STFC (UK) as international partners. It is operated by these agencies in co-operation with ESA and NSC (Norway). C.C. is grateful for support received from the University of Cambridge Overseas Trust and an Isaac Newton Studentship. A.C.S. and R.L.M. received support from NASA's Solar Physics Supporting Research and Technology, Heliophysics Guest Investigators, and Living With a Star programs. H.E.M. acknowledges support from STFC.

References

Aulanier, G., Török, T., Démoulin, P., & DeLuca, E. E. 2010, ApJ, 708, 314
Amari, T., Luciani, J. F., & Aly, J. J. 2004, ApJ, 615, L165
Antiochos, S. K. 1998, ApJ, 502, L181
Antiochos, S. K., DeVore, C. R., & Klimchuk, J. A. 1999, ApJ, 510, 485
Attrill, G. D. R., van Driel-Gesztelyi, L., Démoulin, P., et al. 2008, Sol. Phys., 252, 349
Beger, T. E., & Lites, B. W. 2003, Sol. Phys., 213, 213
Bone, L. A., van Driel-Gesztelyi, L., Culhane, J. L., Aulanieer, G., & Liewer, P. 2009, Sol. Phys., 259, 31
Brooks, D. E., Kurokawa, H., & Berger, T. E. 2007, ApJ, 656, 1197
Chen, P. F., & Shibata, K. 2000, ApJ, 545, 524
Chifor, C., Mason, H. E., Tripathi, D., et al. 2006, A&A, 458, 965
Chifor, C., Tripathi, D., Mason, H. E., & Dennis, B. R. 2007, A&A, 472, 967
Chifor, C., Hannah, I. G., Mason, H. E., et al. 2008, First Results From Hinode ASP Conf. Ser., Proceedings of the conference held 20−24 August, 2007, at Trinity College Dublin, Dublin, Ireland, ed. S. A. Matthews, J. M. Davis, & L. K. Harra (San Francisco: ASP), 397, 164
Culhane, J. L., Harra, L. K., James, A. M., et al. 2007, Sol. Phys., 243, 19
Dere, K. P., Landi, E., Mason, H. E., Monsignori Fossi, B. C., & Young, P. R. 1997, A&AS, 125, 149
Deng, Y., Lin, Y., Schmieder, B., & Engvold, O. 2002, Sol. Phys., 209, 153
Fan, Y., & Gibson, S. E. 2007, ApJ, 668, 1232
Forbes, T. G., & Isenberg, P. A. 1991, ApJ, 373, 294
Forbes, T. G., Linker, J. A., Chen, J., et al. 2006, Space Sci. Rev., 123, 251
Golub, L., Austin, G., Bookbinder, J., et al. 2007, Sol. Phys., 243, 63
Gopalswamy, N., & Thompson, B. J. 2000, J. Atmos. Sol. Terr. Phys., 62, 1457
Green, L. M., Démoulin, P., Mandrini, C. H., & van Driel-Gesztelyi, L. 2003, Sol. Phys., 215, 307
Heyvaerts, J., Priest, E., & Rust, D. M. 1977, Sol. Phys., 53, 255
Handy, B. N., Acton, L. W., Kankelborg, C. C., et al. 1999, Sol. Phys., 187, 229
Harvey, K., & Harvey, J. 1973, Sol. Phys., 28, 61
Hudson, H. S., Lemen, J. R., St. Cyr, O. C., Sterling, A. C., & Webb, D. F. 1998, Geophys. Res. Lett., 25, 2481
Isenberg, P. A., & Forbes, T. G. 2007, ApJ, 670, 1453
Kahler, S. W., Moore, R. L., Kane, S. R., & Zirin, H. 1988, ApJ, 328, 824
Kliem, B., & Török, T. 2006, Phys. Rev. Lett., 96, 255002
Klimchuk, J. A. 2001, in Space Weather, ed. P. Song, H. J. Singer, & G. L. Siscoe, 143
Landi, E., Del Zanna, G., Young, P. R., et al. 2006, ApJS, 162, 261
Leka, K. D., Canfield, R. C., McClymont, A. N., & Van Driel Gesztelyi, L. 1996, ApJ, 462, 547
Li, Y., Lynch, B. J., Stenborg, G., et al. 2008, ApJ, 681, L37
Liewer, P. C., de Jong, E. M., Hall, J. R., et al. 2009, Sol. Phys., 256, 57
Lin, J., Forbes, T. G., & Isenberg, P. A. 2001, J. Geophys. Res., 106, 25053
Linker, J. A., Mikić, Z., Riley, P., Lionello, R., & Odstrcil, D. 2003, Solar Wind Ten, 679, 703
Martin, S. F. 1989, Sol. Phys., 121, 215
Martin, S. F., Livi, S. H. B., & Wang, J. 1985, Aust. J. Phys., 38, 929
Mazzotta, P., Mazzitelli, G., Colafrancesco, S., & Vittorio, N. 1998, A&AS, 133, 403
Moore, R. L., & Sterling, A. C. 2006, Solar Eruptions and Energetic Particles, ed. N. Gopalswamy, R. Mewaldt, & J. Torsti (Washington DC: American Geophysical Union), Geophys. Monogr. Ser., 165, 43
Moore, R. L., & Sterling, A. C. 2007, ApJ, 661, 543
Moore, R. L., Sterling, A. C., Hudson, H. S., & Lemen, J. R. 2001, ApJ, 552, 833
Robbrecht, E., Patsourakos, S., & Vourlidas, A. 2009, ApJ, 701, 283
Rust, D. M. 1976, Sol. Phys., 47, 21
Rust, D. M., & Kumar, ApJ, 464, L199
Scherrer, P. H., Bogart, R. S., Bush, R. I., et al. 1995, Sol. Phys., 162, 129
Shimizu, T., Katsukawa, Y., Matsuzaki, K., et al. 2007, PASJ, 59, 845
Sterling, A. C., & Hudson, H. S. 1997, ApJ, 491, L55
Sterling, A. C., & Moore, R. L. 2004, ApJ, 613, 1221
Sterling, A. C., & Moore, R. L. 2005, ApJ, 630, 1148
Sterling, A., Harra, L. K., & Moore, R. L. 2007a, ApJ, 669, 1359
Sterling, A., Moore, R. L., Berger, T. E., et al. 2007b, PASJ, 59, 823
Su, Y., Golub, L., van Ballegooijen, A., et al. 2007, PASJ, 59, 785
Tan, C., Chen, P. F., Abramenko, V., & Wang, H. 2009, ApJ, 690, 1820
Tsuneta, S., Ichimoto, K., Katsukawa, Y., et al. 2007, Sol. Phys., 249, 167
Uchida, Y., McAllister, A., Strong, K. T., et al. 1992, PASJ, 44, L155
van Ballegooijen, A. A., & Martens, P. C. H. 1989, ApJ, 343, 971
van Driel-Gesztelyi, L. 2009, in Cosmic Magnetic Fields: from Planets, to Stars and Galaxies, ed. K. G. Strassmeir, A. G. Kosovichev, & J. Beckmann, IAU Symp., 259
van Driel-Gesztelyi, L., et al. 2002, J. Atmos. Sol.-Terr. Phys., 62, 1437
Veronig, A. M., Temmer, M., & Vršnak, B. 2008, ApJ, 681, L113
Wang, H., Gallagher, P., Yurchyshyn, V., Yang, G., & Goode, P. R. 2002, ApJ, 569, 1026
Young, P. R., & Mason, H. E. 1997, Sol. Phys., 175, 523
Young, P. R., Del Zanna, G., Mason, H. E., et al. 2007a, PASJ, 59, 857
Young, P. R., Del Zanna, G., Mason, H. E., et al. 2007b, PASJ, 59, 727
Young, P. R., Watanabe, T., Hara, H., & Mariska, J. T. 2009, A&A, 495, 587
Zhang, J., & Wang, J. 2002, ApJ, 566, L117
Zhang, Y., Zhang, M., & Zhang, H. 2008, Sol. Phys., 250, 75
Zirin, H. 1988, Astrophysics of the Sun (Cambridge: Cambridge Univ. Press)